Exp Fluids (2013) 54:1530
DOI 10.1007/s00348-013-1530-6

RESEARCH ARTICLE

Experimental study of entrainment and interface dynamics in a gravity current

Dominik Krug · Markus Holzner · Beat Lüthi · Marc Wolf · Wolfgang Kinzelbach · Arkady Tsinober

Received: 11 February 2013 / Revised: 9 April 2013 / Accepted: 22 April 2013 / Published online: 8 May 2013

Abstract The special case of entrainment in a stratified flow, relevant to many geophysical flows such as oceanic overflows, so far has not been studied experimentally in terms of small-scale aspects around the turbulent/non-turbulent interface. In view of the fact that existing engineering concepts perform unsatisfactorily in practice, a new gravity current facility was designed with the goal to gain understanding of how stratification affects interfacial physics. Here, we present the design of the new setup and give details on the turbulence enhancement in the inflow and the refractive index matching technique used. Validation measurements ensure that there is negligible backflow and an essentially irrotational flow outside the current. Measurements via particle image velocimetry of a flow with inflow Reynolds and Richardson numbers of $Re_0 \approx 4{,}000$ and $Ri_0 = 0.22$ are reported. An analysis in a laboratory frame agrees well with flow features reported in the literature, i.e., a streamwise invariant top-hat velocity scale and a Reynolds stress distribution are matched closely by a mixing length model. In a second step, the instantaneous interface position is determined based on a threshold on the normal enstrophy component. An investigation in a frame of reference conditioned on the interface position reveals a strong interfacial shear layer that is much more pronounced than the one observed in jet flows. Its thickness is about two times the Taylor microscale. The data moreover suggest the existence of a fairly strong interfacial density jump across the shear layer. The entrainment parameter is estimated at $E \approx 0.04$ congruently from the evaluations in laboratory and conditioned frame, respectively.

D. Krug (✉) · M. Holzner · B. Lüthi · M. Wolf · W. Kinzelbach
Institute of Environmental Engineering, ETH Zurich, 8093 Zurich, Switzerland
e-mail: krug@ifu.baug.ethz.ch

A. Tsinober
The Iby and Aladar Fleischman Faculty of Engineering, Tel Aviv University, 69978 Ramat Aviv, Israel

1 Introduction

Entrainment is a ubiquitous phenomenon in engineering as well as environmental flows. Among many other occurrences, see, e.g., Simpson (1999) and references therein, the special case of gravity current entrainment has received extensive attention since it is the essential process governing so-called oceanic overflows. In these flows, dense water formed through cooling or evaporation in marginal seas travels down a sloping bottom into deeper ocean basins. The entrainment process happens on length scales much smaller than the highest resolution affordable in large-scale numerical investigations. Yet, since outflow from overflows contributes strongly to deepwater formation in the oceans (Rahmstorf 2002), the correct representation of gravity current entrainment is a crucial element of any ocean general circulation model (Legg et al. 2009).

The dense gravity current flow can be pictured as a plume whose rise or fall is deflected by a sloping wall. Our experimental setup essentially resembles the one of Odier et al. (2009). For practical reasons, the flow situation in the present experiment illustrated in the sketch of Fig. 1 was reversed to the overflow case. This is admissible within the Boussinesq approximation for small density differences (i.e., $\Delta\rho/\rho \ll 1$) which usually applies for the case of gravity currents. The study focuses on the steady-state current that establishes some time after the current head has passed the domain.

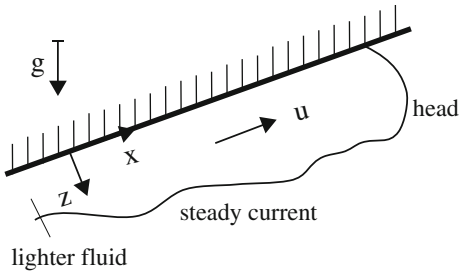

Fig. 1 Sketch of a gravity current flowing upwards

In the coordinate system indicated in Fig. 1 with u and w denoting the velocity components in x and z directions, respectively, the steady-state equation for the Reynolds averaged streamwise momentum reads

$$U_i \frac{\partial U}{\partial x_i} = \frac{\partial \overline{p}}{\partial x} + \nu \frac{\partial^2 U}{\partial x_i^2} - \frac{\partial \overline{u' u_i'}}{\partial x_i} - g' \sin \alpha. \tag{1}$$

Here and in the following, the temporal average is indicated by overbars or capital letters, e.g., $u(\mathbf{x}, t) = U(\mathbf{x}) + u'(\mathbf{x}, t)$. In deriving Eq. 1, use of the Boussinesq approximation has been made, such that the (small) density difference $\Delta\rho = \rho_0 - \rho$ does not appear in the convective terms and is absorbed in the reduced gravitational acceleration $g' = g\Delta\rho/\rho_0$. In their recent study on gravity currents, Odier et al. (2009) concluded that a good closure for the $\overline{u'w'}$-component of the Reynolds stress tensor occurring in Eq. 1 can be obtained using a mixing length model. That is $\overline{u'w'} = -l_m^2 \left|\frac{\partial U}{\partial z}\right| \frac{\partial U}{\partial z}$, where l_m is a free parameter referred to as the mixing length. The following integral "top-hat" scales are commonly defined to characterize the flow field based on mass and momentum flux:

$$U_T h = \int_{z=0}^{\infty} u \mathrm{d}z \quad \text{and} \quad U_T^2 h = \int_{z=0}^{\infty} u^2 \mathrm{d}z, \tag{2}$$

where U_T and h are the top-hat velocity and current height, respectively. Buoyancy forces counteract the mixing process at the interface, whereas shear forces enhance turbulent mixing. Their relative strength is a defining property of the flow field and defines the dimensionless Richardson number

$$Ri = \frac{g' h \cos\alpha}{U_T^2} = \frac{A \cos\alpha}{U_T^3}, \tag{3}$$

where the buoyancy flux $A = g_0' U_0 g d = \text{const.}$ is a conserved quantity and can therefore be derived from the inflow values, U_0, g_0', and the inlet height d. From the conservation of mass, it follows for the mean entrainment velocity u_e that

$$u_e = \frac{\partial (U_T h)}{\partial x}. \tag{4}$$

Applying the Morton–Taylor–Turner entrainment hypothesis, namely $u_e \propto U_T$, yields the expression for the entrainment coefficient $E = \frac{u_e}{U_T} = \frac{1}{U_T}\frac{\partial (U_T h)}{\partial x}$. It has been observed that shortly after its release the flow adjusts to an equilibrium state in which U_T is no longer a function of x (Ellison and Turner 1959). The entrainment coefficient is then simply given by $E = \frac{\partial h}{\partial x}$. Ellison and Turner (1959) determined E to be a function of the Richardson number only and later Turner (1986) gave the empirical expression valid for $0 \leq Ri \leq 0.8$

$$E_{\text{fit}} = \frac{0.08 - 0.1Ri}{1 + 5Ri}. \tag{5}$$

Note that this fit predicts vanishing entrainment for $Ri > 0.8$ which is not in line with observations in natural flows (Arneborg et al. 2007). While the above-mentioned global approaches follow very intuitive engineering concepts, we would like to try to advance the subject of gravity current entrainment by exploiting knowledge on the physics governing the mixing process. Since Corrsin and Kistler (1954) introduced the notion of a sharp interface dividing turbulent rotational from non-turbulent irrotational fluid, there have been a number of numerical (Bisset et al. 2002; Mathew and Basu 2002; da Silva and Taveira 2010) and experimental studies (Westerweel et al. 2002; Holzner et al. 2006; Anand et al. 2009; Wolf et al. 2012; Philip and Marusic 2012) on various flow types focussing on the dynamics around the turbulent/non-turbulent interface (TNTI). However, up to this point, a similar experimental investigation into small-scale processes in the proximity of the TNTI in stratified flow is lacking. In view of the importance of this issue, the intention to fill this gap provided the motivation to set up the experiment presented in the following.

The analysis with respect to the TNTI requires the determination of the instantaneous interface position z^i. Details on this step will be given in Sect. 2.3. Once z^i is known, flow quantities can be described in a coordinate system relative to the interface by defining $\tilde{z} = z - z^i$. Averages taken in the system conditioned on the interface position are indicated by angular brackets, and all quantities conditioned on the interface position marked by a tilde, e.g., $u(\mathbf{x}, t) = \langle U(\mathbf{x}) \rangle + \tilde{u}(\mathbf{x}, t)$.

In this paper, we will first introduce the design of the new setup along with details on the measurements (Sect. 2). Verification measurements on the general flow field will be shown in Sect. 3 and comparisons to a recent study by Odier et al. (2009) will be made. The results section features a conventional analysis in the laboratory frame (Sect. 4.1). Moreover, we will present first results of a local analysis following the work by Westerweel et al. (2009) on the TNTI of a jet flow at the end of this paper in Sect. 4.2.

2 Method

2.1 Experimental setup

The gravity current in this study is realized by conveying lighter fluid upward along the sloping top of an inclined tank that is filled with a denser fluid. This choice—along with other aspects of the design—was inspired by the setup used in Odier et al. (2009). A schematic of our facility is shown in Fig. 2. The flow tank measures 2 m in length and 0.5 m in width and height, respectively. While the design of the support of the tank allows for a continuous variation of the tilt angle between 0° and 90° to the horizontal, the slope was kept fixed at $\alpha = 10°$ for the measurements reported here. The top and sidewalls of the tank are made of glass, while the bottom and end parts consist of aluminum plates. The inflow enters through an opening in one of the end walls ($d = 5$ cm high and 45 cm wide) the upper edge of which is at level with the inside of the top glass plate. The tank is filled completely at all times and excessive mixed fluid leaves the domain via an outflow opening (10 cm × 45 cm) at the side opposite to the inflow. In order to prevent backflow and to eliminate the influence of the finite dimensions of the tank as much as possible, entrained dense fluid is resupplied at the bottom of the flow tank. The working fluids of the experiment are index-matched solutions of water and salt (denser fluid) and water and ethanol (lighter fluid). Both fluids are freshly prepared for each run in separate containers with a capacity of 1,000 l each. The lighter fluid enters the tank via a frequency controlled pump and a diffusor (see next paragraph), whereas the salt solution is supplied through a constant head tank. From there, the heavier fluid enters two pipes that run along the length at the bottom of the tank (see Fig. 2). Each of these pipes (outer diameter 63 mm) is fed from both ends and features around 2,000 holes (1 mm wide) spread across the top part of their perimeter to distribute the flow evenly. The pipes are wrapped in two layers of porous foam (10 ppi/10 mm thick and 20 ppi/5 mm) in order to break down the small jets issuing from the holes.

Inflow treatment The transition to turbulence via the growth of Kelvin-Helmholtz instabilities in the shear layer takes around 150 shear time scales until breakdown (Smyth and Moum 2000). There are additional instabilities of the wall boundary layer, but relying on transitional mechanisms is prohibitive in the experiment as it would require an impractically long tank. Therefore, it was decided to enhance the turbulence level by means of active grids in the inflow section similar to Odier et al. (2009). At the same time, in accordance with the 2D nature of the flow, the spanwise distribution of the velocity at the inflow should be as uniform as possible. To achieve this, significant effort was spent on the inflow section and the resulting design is presented in the following.

Prior to entering the tank, a diffusor equipped with four perforated plates (see Fig. 3b) to prevent separation ensures that the incoming pipe flow is expanded thoroughly. Afterward, the flow passes an array of four 'flapping grids' (see Fig. 3c) that are used to control and enhance the turbulence level. Each grid is driven by a 240 W motor. Based on a 100 Hz base signal, their rotational direction is switched randomly and independently of each other. The frequency of the base signal is chosen, such that the grids usually perform less than a full rotation minimizing the disturbance to the spanwise distribution of mean streamwise velocity—hence the name 'flapping grids.' An array of three perforated plates just before the opening of the tank completes the inflow treatment. The layout of the inflow section is shown in Fig. 3a.

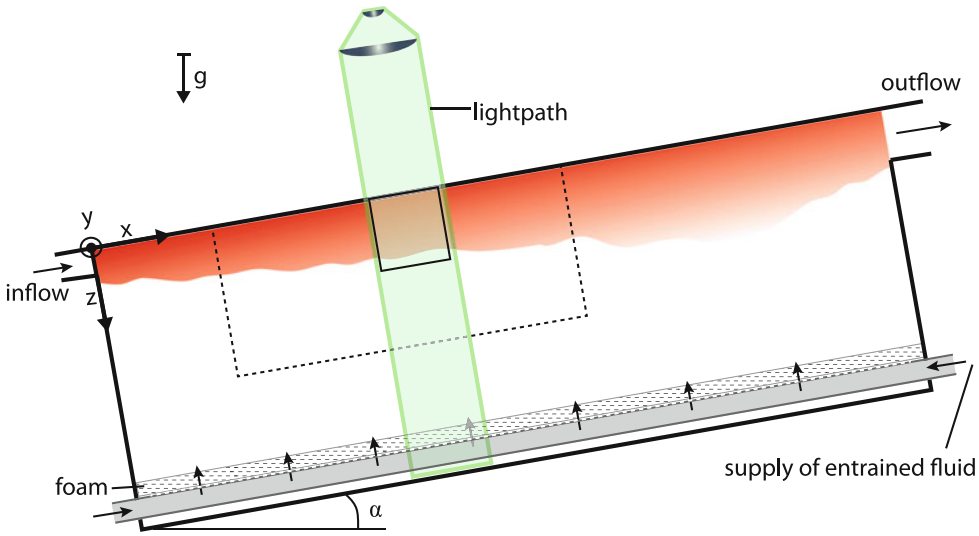

Fig. 2 Schematic of the experimental setup. The *red area* indicates lighter fluid that flows along the top wall of the tank; mixed fluid leaves the tank through an opening at the higher end. Entrained fluid is replaced through pipes at the bottom. The two different PIV investigation domains are approximately indicated by rectangles (*dashed*: large domain for flow field validations, *solid*: small domain for turbulence and TNTI study). Also indicated is the lightpath for the small domain

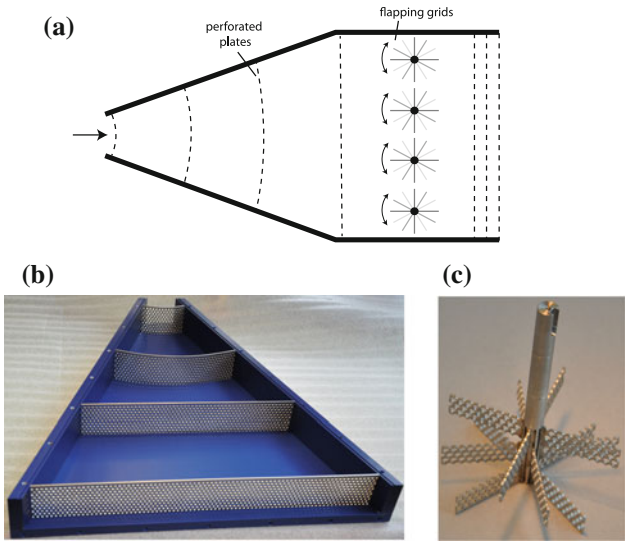

Fig. 3 Sketch of the inflow section (**a**) along with images of the opened diffusor (**b**) and a single grid (**c**)

Additionally, the flow rate is kept constant by placing the pump in a closed loop control with feedback from a flowmeter. This ensures a steady inflow even as the water level in the container is dropping.

Index matching Local variations of the refractive index (RI) in a flow can severely hamper optical measurement techniques such as particle image velocimetry (PIV), laser-induced fluorescence, or particle tracking velocimetry or even render their application impossible should they become too large. The issue can be overcome in flow applications with variable density by RI matching, a method that dates back to McDougall (1979). Instead of using a single stratifying agent, it makes use of a pair of solutes that differ in their impact on density and RI. Thus, it is possible to find a ratio of solute concentrations that—at a given density difference—will result in matching refractive indices. From the choice of candidate pairs reported in the literature, Daviero et al. (2001) identified a combination of ethanol and sodium chloride (simply referred to as 'salt' from here on) to be the most suitable for experiments of a larger scale, and it is therefore also chosen for this study.

Unfortunately, it turned out that the parameters determined by Daviero et al. (2001) did not fully agree with our case, and all the measurements were therefore repeated. A possible explanation for this is differences caused by the additives contained in the denatured ethanol used here. Their presence also reflects itself in a slightly higher density of 805.2 g l^{-1} with respect to the literature value of 789.3 g l^{-1} for pure ethanol. The refractometer used (Misco Palm Abbe) to measure the RI has an accuracy of ± 0.0001; the density could be determined within $\pm 0.1\,\mathrm{g\,l^{-1}}$ using a pycnometer and a precision scale. Figure 4 shows the resulting densities and RIs for different concentrations of ethanol and salt

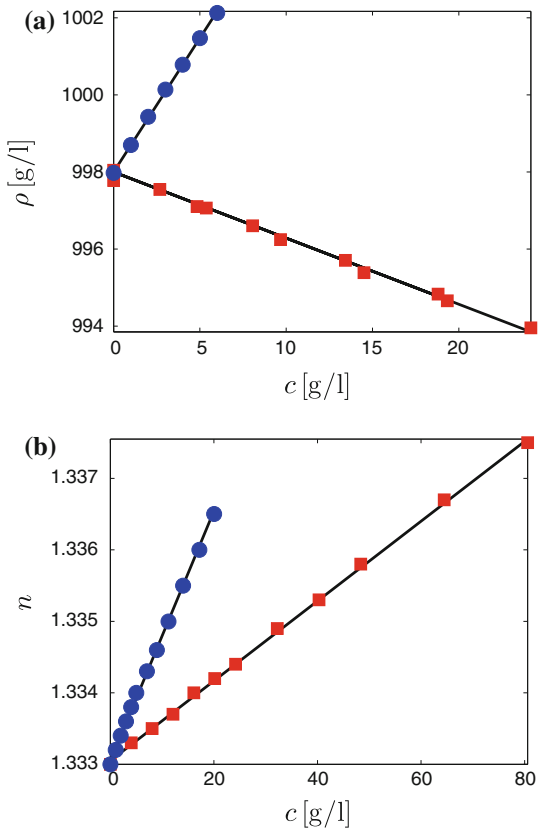

Fig. 4 Measurements of density (**a**) and refractive index (**b**) for salt (*blue circles*) and ethanol (*red squares*) solutions. The *black lines* represent linear fits to the data

solutions. The data can be very well represented by linear fits (black lines in the figure) in the ranges investigated.

The fits result in the following expression for the density difference of the two solutions

$$\Delta\rho = 0.6949 c_{\mathrm{salt}} + 0.1716 c_{\mathrm{eth}}, \tag{6}$$

where c_{salt} and c_{eth} denote the solute concentrations of salt and ethanol, respectively, and all quantities are given in g l^{-1}. Requiring the change of RI, Δn, to be equal for both solutions and using the linear fits obtained from the data in Fig. 4b yields a condition for the ratio of the solute concentrations:

$$\Delta n_{\mathrm{salt,eth}} = 1.7467 \cdot 10^{-4} c_{\mathrm{salt}} = 0.5585 \cdot 10^{-4} c_{\mathrm{eth}} \tag{7}$$

Finally, combining Eqs. 6 and 7 gives the solute concentrations in the index-matched case at a given density difference:

$$c_{\mathrm{salt}} = 0.8119 \Delta\rho \tag{8}$$

and

$$c_{\mathrm{eth}} = 2.5391 \Delta\rho \tag{9}$$

As mentioned above, the coefficients in Eqs. 8 and 9 differ slightly from the ones reported in Daviero et al. (2001).

Experimental procedure Before each experiment, the tank and both supply containers were filled with tap water that is subsequently heated up to equilibrium with the room temperature in the laboratory. A slider at the inlet to the tank is then closed in order to separate the inflow section from the tank until the start of the actual experiment. In this way, it is possible to circulate lighter and denser fluids independently of each other in closed loops while the stratifying agents are added up to the required amount. A typical density difference of 2.5 g l^{-1} requires about 7 l of ethanol and 3.3 kg of salt for the preparation of 1,000 l lighter and 1,500 l of denser fluid. On top of the circulating flow, the mixing is additionally promoted by stirrers in the supply containers and, in addition, switching on the flapping grids provides mixing in the diffusor. Just before the flow is started, it is again checked that the temperature of the two solutions is equal within 0.2°C. This is crucial since the temperature affects both the RI (about 0.0001 $°C^{-1}$) and the density (0.1 g $l^{-1}°C^{-1}$). At the same time, the actual density of the solutions is measured. From the state with solutions circulating separately, the gravity current flow is initiated through the following steps: at first, the grids are switched on, then the control valves at the ends of the two pipes are switched to the previously determined appropriate setting for the desired flow conditions. Finally, the set point of the inflow control loop is changed to the required inflow for the experiment and the slider is opened.

Some important flow parameters of the experiments as determined at the inlet are presented in Table 1.

2.2 Measurement technique

Velocity data were obtained through PIV measurements in the centerplane of the tank aligned with the x- and z-axis. For this purpose, the flow was seeded with 45 µm neutrally buoyant polystyrene particles (Vestosint 2,162, resulting in a Stokes number $St \approx 0.001$) and illuminated using a continuous 20 W argon ion laser (514 nm line). The laser beam was expanded into a light sheet using two cylindrical lenses while the thickness was adjusted using a long focal spherical lens to somewhat below 1 mm. The rectangular measurement domain aligns with the top wall and extends 12 cm into the flow (z-direction) covering a streamwise interval from $x = 45.3$ to 57.3 cm. Particle images were recorded using a high-speed camera (Photron SA5) with a resolution of 1,024 × 1,024 pixels set to a frame rate of 250 Hz. The analysis of the images was performed using the code *JPIV 2.1*[1]. A multigrid scheme with a final interrogation window of 16 × 16 pixels with an overlap of 50 % was employed. This results in a vector spacing of approximately 1.0 mm. With the estimate of the Kolmogorov length scale $\eta \approx 0.3$ mm obtained in Sect. 4.2, this corresponds to a spatial resolution of 3.3η. Since a time interval of $\Delta t = 1/250$ s = 4 ms proved to be oversampling the data, images taken at a time t were cross-correlated with the one taken at $t + 3\Delta t$ reducing the temporal resolution to 83.3 Hz. Few outliers were detected using a normalized median test and replaced by the local median. Assuming a displacement error of about 0.1 pixel yields an estimate of about 1 mm s^{-1} for the measurement error. A series of 10,000 frames corresponding to 40 s or 27 shear timescales d/U_0 were evaluated. Figure 5 shows a snapshot of the velocity fields obtained.

Table 1 Flow parameters determined at the inlet

U_0	7.41 cm s^{-1}
$\Delta\rho_0$	2.5 g l^{-1}
α	10°
d	5 cm
$Re = U_0 d/\nu$	3,700
$Ri_0 = g'_0 d \sin\alpha / U_0^2$	0.22
$Re_{\lambda,0} = u'_0 \lambda/\nu$	≈100

Details on the Taylor Reynolds number, $Re_{\lambda,0}$, are given in Sect. 3.1

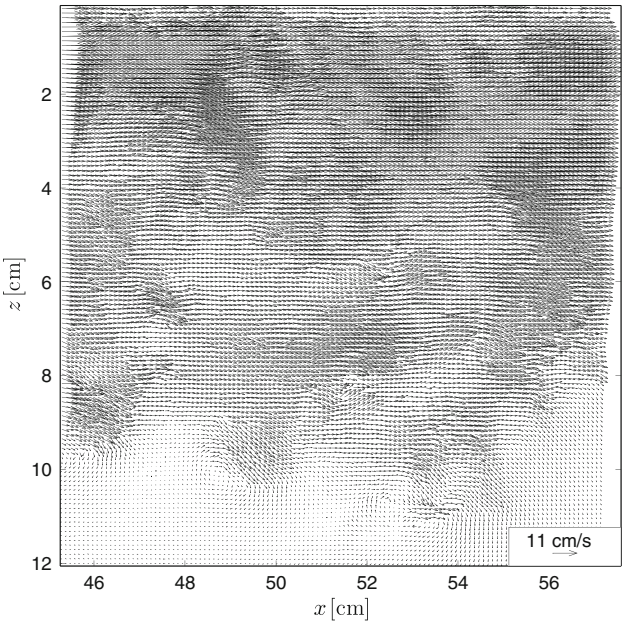

Fig. 5 Snapshot of the velocity field obtained from the PIV measurements (small domain)

Preliminary measurements of the entire flowfield were performed on a larger window as indicated in Fig. 2 (dashed rectangle) covering a great portion of the tank. In this case, a domain of size $x = 22$–99 cm and $z = 0$–40 cm was observed using two cameras setup next to each other and recording simultaneously. Their images were merged later on. For this case, the smallest window size was set to

[1] This open source code is publicly available from http://www.jpiv.vennemann-online.de/.

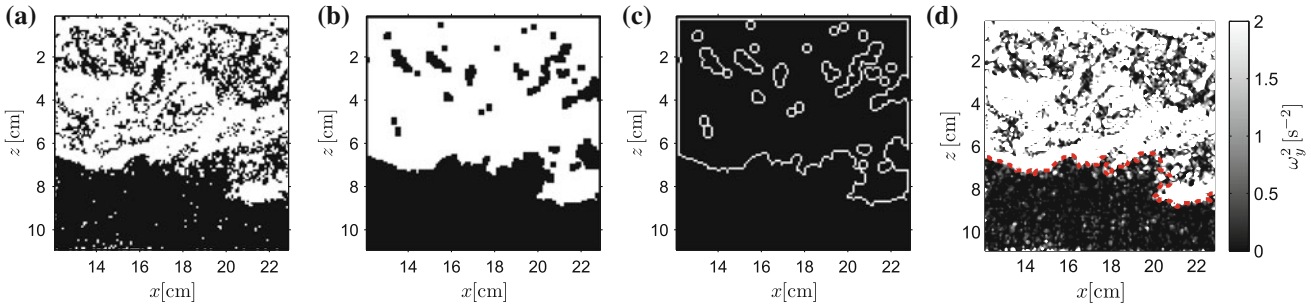

Fig. 6 Illustration of the interface detection. The enstrophy field is transformed into a binary field (**a**) and subjected to a morphological *closing* operation (**b**). The lower boundary of the remaining patch forms the interface (**c**). Figure **d** shows the interface obtained superimposed onto a contour plot of instantaneous enstrophy

20 × 20 pixels. The vector spacing of 10 pixels translates to a resolution of 4.4 mm. The frame rate of the recording was lowered to 50 Hz, but still two consecutive frames were skipped in the analysis.

From the PIV velocity fields, the normal component of vorticity, $\omega_y = \frac{\partial u}{\partial z} - \frac{\partial w}{\partial x}$, was calculated using a least squares approximation scheme for the gradients.

2.3 Detection of the turbulent/nonturbulent interface

Westerweel et al. (2009) used the concentration of a dye as a marker for the turbulent zone. However, since then it has instead become popular to define the interface by a threshold on vorticity, or its square, enstrophy, directly whenever possible. This choice is not made out of experimental convenience but appears only natural as vorticity is the very quantity commonly used to distinguish turbulent from non-turbulent motion. Consequently, the interface was defined by a threshold on the available normal enstrophy component, ω_y^2 (for the sake of brevity in the following simply referred to as 'enstrophy') in this study. For reasons given in Sect. 4.2, a threshold value of $\omega_{y,0}^2 = 1\,\mathrm{s}^{-2} \approx (0.95h/U_T)^2$ was selected here, and the interface position z^i was determined according to the following steps:

1. First, the enstrophy field is transformed into a binary field by assigning the value '0' where $\omega_y^2(x, z) < \omega_{y,0}^2$ and '1' if $\omega_y^2(x, z) \geq \omega_{y,0}^2$ (see Fig. 6a).
2. Next, the morphological *closing* operation with a [3 × 3] kernel is applied closing holes within the turbulent and removing noise pixels in the non-turbulent region (Fig. 6b).
3. Finally, only the pixels forming the boundaries are kept, and the interface position is determined by tracing the continuous lower boundary, using MATLAB native function *bwtraceboundary* (Fig. 6c).

A typical result of this procedure is plotted into a contour plot of instantaneous enstrophy in Fig. 6d. To avoid ambiguities, only x-positions providing a unique value of $z^i(x)$ were considered in the subsequent analysis.

3 Flow characterization

3.1 Inflow

In order to gauge the effectiveness of the inflow treatment, PIV measurements were conducted about 5 cm downstream of the inlet in a xy-plane located midway between the top glass wall and the lower edge of the inlet and extending over the entire width of the tank. The intensity of the turbulence can be controlled by changing the power applied to the grids. The turbulence level was characterized in terms of the Taylor Reynolds number defined as $R_\lambda = u'\lambda/\nu$ where the Taylor microscale was estimated from $\lambda = u'\sqrt{15\nu/\epsilon}$ and the local dissipation from $\epsilon = u'^3/L$. As an approximation of the length scale L, the height $d = 5$ cm of the inlet was chosen.[2] Three different power settings for the motors driving the grids were tested. The results along with a curve obtained with the grids switched off are presented in Fig. 7. It shows that with the help of the grids, R_λ in the inflow can effectively be controlled within a range of about $50 < R_\lambda < 120$. Data presented in this study were obtained at the intermediate power setting at around $R_\lambda \approx 100$.

To check whether the spanwise distribution of U is in fact uniform even with the grids turned on, mean profiles obtained with (solid line) and without activating the grids (dashed lines) are presented in Fig. 8. The profiles are normalized using the mean inflow velocity U_0 obtained by dividing the measured flow rate by the area of the inlet. In the case where the grids are turned off, there is almost no variation in the spanwise direction indicating the effectiveness of the diffusor in providing a homogenous inflow. Since the wall-normal profile at this stage is expected to

[2] Note that with otherwise similar dimensions Chen et al. (2007) report an integral length as high as $L = 8$ cm resulting in a higher estimate of R_λ.

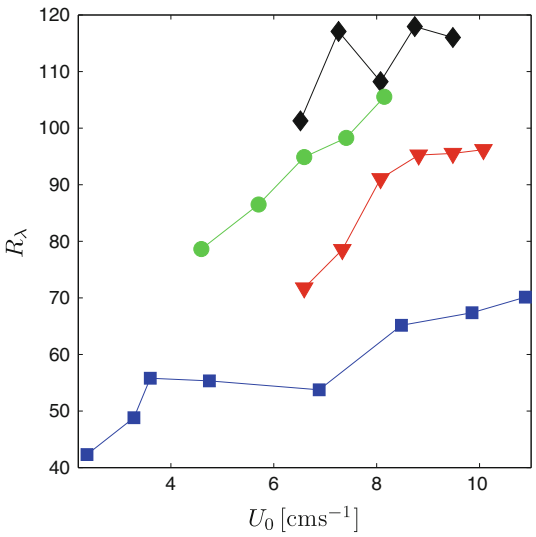

Fig. 7 Taylor Reynolds number in the inflow at different inflow velocities and grid settings; *blue squares*: grids off, red triangles, *green dots*, and *black diamonds*: grids switched on at low, intermediate, and high-power settings, respectively,

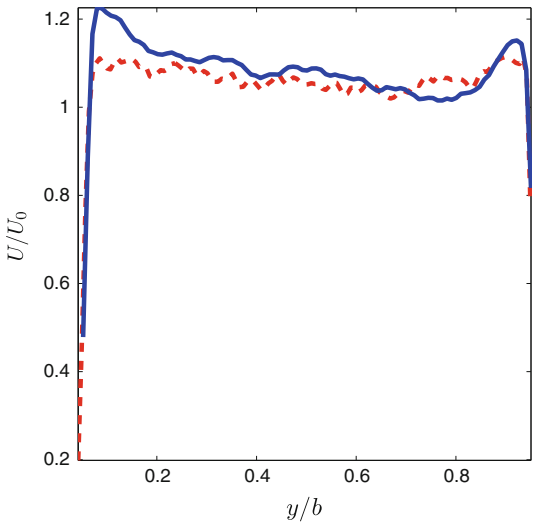

Fig. 8 Spanwise inflow profiles without turbulence enhancement (*dashed red line*) and with grids turned on (*solid blue line*, intermediate power setting) normalized by the mean inflow velocity U_0 and the width b of the tank, respectively,

resemble channel flow, the velocity measured in the centerplane is slightly higher than U_0. Switching on the grids in the flapping mode described above alters the spanwise distribution only slightly. The most notable change is a shift of momentum toward the edges of the flow that, however, remains below 10 % of U_0. This should not be of any additional concern with respect to the quasi-2D nature of the flow away from the side walls since the outer parts are subjected to boundary effects anyway.

3.2 Large-scale flow investigation

Unless accounted for by any counter measures, starting the gravity current flow in a finite tank will result in backflow along the bottom of the tank. This is highly undesirable, as the developing backflow renders important parameters of the flow, such as shear, time dependent. Even worse, recirculating lighter fluid might change the stratification properties within the test section uncontrollably. The design employed to cope with this problem follows the one already used successfully by Ellison and Turner (1959): the amount of fluid entrained by the gravity current is injected at the bottom of the tank. As mentioned in Sect. 2.1, this is implemented in the present setup using two pipes located at the bottom of the tank. This method, however, requires prior knowledge on what the correct resupply rate (or in more practical terms the correct settings of the valves on each end of the pipes) for given flow parameters should be. To determine the proper valve settings, PIV measurements on the large volume were performed with different valve settings, and the one resulting in minimum backflow streamwise flow was chosen as the correct one. As Fig. 9a proves, it was possible to achieve almost zero streamwise velocity in regions outside the gravity current on a domain covering more than half the tank in streamwise direction, i.e., within the zone most suitable for further investigations. Judging from the emptying of the respective supply containers, it shows that the required flow rate for the resupply of heavy fluid is of the same order as the inflow of lighter fluid. Still, perturbations originating from the pipes remain very weak, and no vortical motions are present in the proximity outside the gravity current (see Fig. 9b).

To put these results into perspective, they are compared to recent results of a similar experiment with matching parameters conducted at Los Alamos National Laboratory (abbreviated LA in the following) (Chen et al. 2007; Odier et al. 2009, 2012). Since the top-hat scales U_T and h are not available for the LA setup, the velocity profiles presented in Fig. 10 are normalized by the inflow parameters U_0 and d. In general, the profiles agree fairly well, however, the backflow in the LA setup seems to alter the velocity distribution somewhat in the mixing region. Changes in streamwise direction are small and mainly concern the region close to the wall where buoyancy appears to accelerate the flow.

A second type of flow features that can be compared is wall-normal profiles of the Reynolds stresses $\overline{u'w'}$ shown in Fig. 11. Also here, the agreement between the two experiments is reasonable in the turbulent region. The fact that the values of $\overline{u'w'}$ in regions outside the main flow are very close to zero corroborates the conclusion drawn already from Fig. 9b, i.e., that no measurable turbulence originates

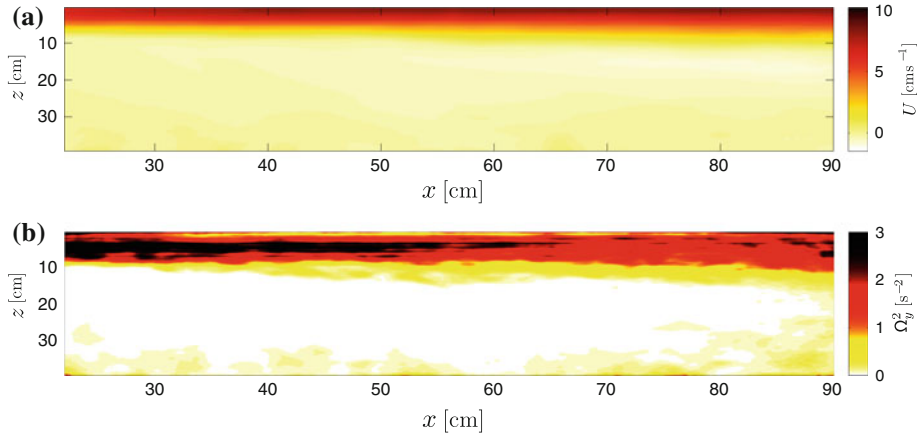

Fig. 9 Contour plots of mean streamwise velocity U (**a**) and mean normal enstrophy component Ω_y^2 (**b**) obtained on the large PIV window

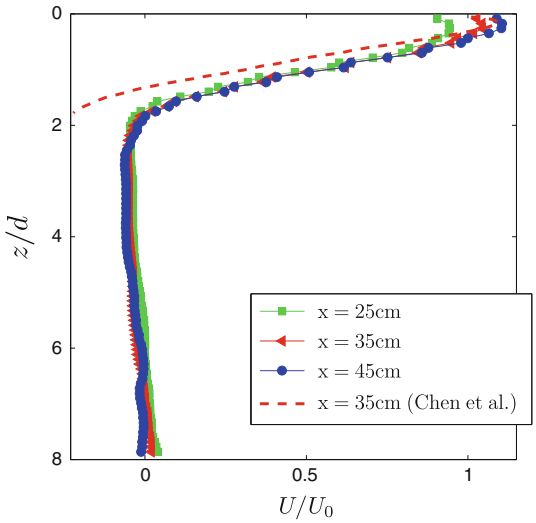

Fig. 10 Profiles of mean streamwise velocity at different streamwise locations. Data of the Los Alamos setup are taken from Chen et al. (2007)

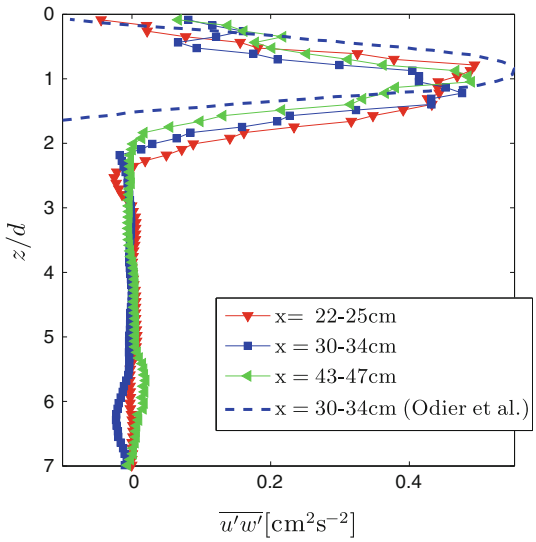

Fig. 11 Wall-normal profiles of the Reynolds stress component $\overline{u'w'}$. Data of the Los Alamos setup taken from Odier et al. (2012)

from the pipes and the flow outside the gravity current can in fact be considered irrotational.

4 Results and discussion

4.1 Analysis in the laboratory frame

Figure 12 displays the streamwise development of top-hat velocity and length scale as defined in Eq. 2. Congruently with the observations by Ellison and Turner (1959), U_T remains almost constant at a value of 6.95 cm s^{-1} while h increases steadily with x at an approximately linear rate. In order to provide a unique length scale for the entire domain, we use the mean value of $h = 6.64$ cm in the following which seems justified given the modest change of h within the domain. With the definitions in Eqs. 3 and 4, it follows for the local Richardson number that $Ri = 0.257$ and the mean entrainment velocity $u_e = -0.28$ cm s^1 (defined positive in positive z-direction). The corresponding entrainment coefficient $E = |u_e|/U_T = 0.04$ is somewhat higher than the one determined from the fit in Eq. 5 $E_{\text{fit}}(Ri = 0.257) = 0.024$. A possible explanation for this disagreement, though almost covered by the scatter in the data of Ellison and Turner (1959), could be explained by the presumably higher turbulence level in the present study since Ellison and Turner (1959) did not take any measures to enhance turbulence in the inflow.

The time-averaged velocity profile along with its gradient with respect to the wall-normal coordinate is shown in Fig. 13. The velocity profile features a maximum quite close to the wall and approaches zero around 1.4 z/h. Apart from the boundary layer that is not the subject of further investigations here, the magnitude of the gradient reaches a maximum between $z/h = 0.4$ and $z/h = 0.8$ indicating less intensive mixing in this zone compared to the regions further from the wall.

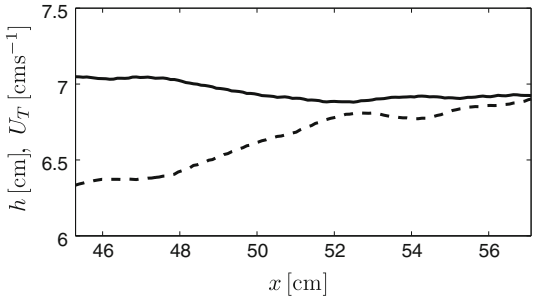

Fig. 12 Experimental results for U_T (*solid line*) and h (*dashed line*) as defined in Eq. 2

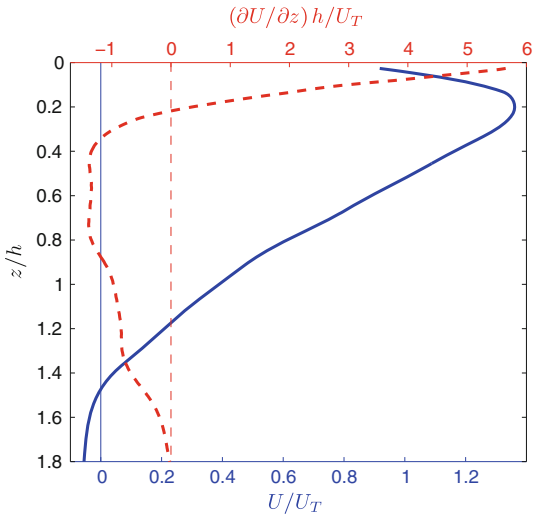

Fig. 13 Mean profile of streamwise velocity (*blue solid line*) and its derivative with respect to z (*dashed red line*)

An investigation along the lines of Odier et al. (2009) is presented in Fig. 14. The figure shows the available Reynolds stress component plotted versus $(\frac{\partial U}{\partial z})^2$, a scaling suggested by the mixing length model. In agreement with the findings by Odier et al. (2009), this model is seen to fit also the present data set quite well. The mixing length of $l_m = 0.57$ cm resulting from a fit to the data is in the range of data obtained by Odier et al. (2012) in similar conditions ($l_m = 0.45$ cm and $l_m = 0.6$ cm in configurations 1 and 2 therein, respectively).

4.2 Local analysis with respect to the TNTI

In the following, conditional averages for various quantities are compared to those obtained in an unstratified jet flow by Westerweel et al. (2009). Clearly, the fundamental differences between the two flows forbid a one to one comparison of the results, especially closer to the wall of the gravity current or the centerline of the jet, respectively. Since, however, the differences in the vicinity of the TNTI are mainly due to the stratification, the jet flow is

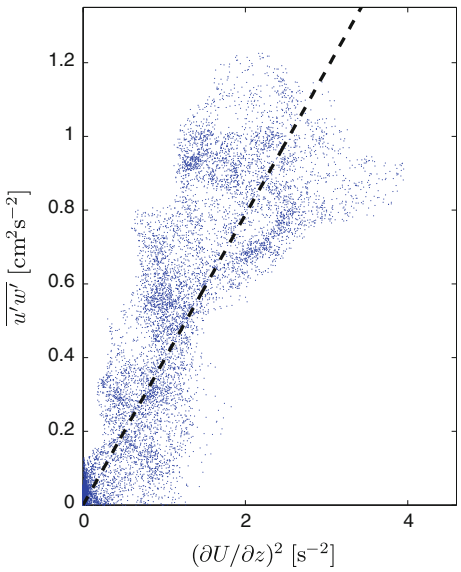

Fig. 14 Scatter plot of $\overline{u'w'}$ for $z/d > 0.4$. From the slope of the linear fit to the data (*dashed line*), it follows that $l_m = 0.57$ cm; data for $z < 0.5d$ (i.e., the wall boundary layer) was omitted

considered a valuable benchmark to gauge buoyancy effects on the gravity current in the interfacial region. In the original publication, the jet results are normalized by the centerline velocity, U_c^{jet} and the velocity halfwidth, b_u^{jet}. Integration of the jet profile according to Eq. (2) yields the relations used to rescale the data: $U_T^{\text{jet}} = U_c^{\text{jet}}/2$ and $b_u^{\text{jet}} = h^{\text{jet}}$ where the superscript 'jet' is dropped in the following.

The results for the mean vorticity conditioned on the interface position are displayed in Fig. 15. Note that positive values $\tilde{z}$ indicate regions outside the turbulent zone here. As mentioned earlier, Westerweel et al. (2009) detected the interface by means of a dye concentration instead of enstrophy. Therefore, it is not surprising that the present data show a sharper increase in vorticity at the interface position. The fact that this increase is very strong implies that the interface position determined is greatly insensitive of the threshold value justifying the somewhat arbitrary choice made for $\omega_{y,0}^2$ in Sect. 2.3. There is a remarkable spike in the gravity current data just inside of the interfacial layer that is much more pronounced than the one obtained in a jet. It has got a width of about 0.15 h and its peak reaches about 2.5 times the vorticity value within the ensuing turbulent region between $-0.15 > \tilde{z}/h > -0.9$ in which jet and gravity current agree closely. As reasoned above, this agreement falls apart for $\tilde{z}/h > -0.9$ where the differences in the flow structures dominate.

Conditional profiles of further quantities are collected in Fig. 16. The streamwise velocity profile in Fig. 16a features a steeper gradient—commonly referred to as 'velocity jump' ΔU—in a region congruent with the appearance of

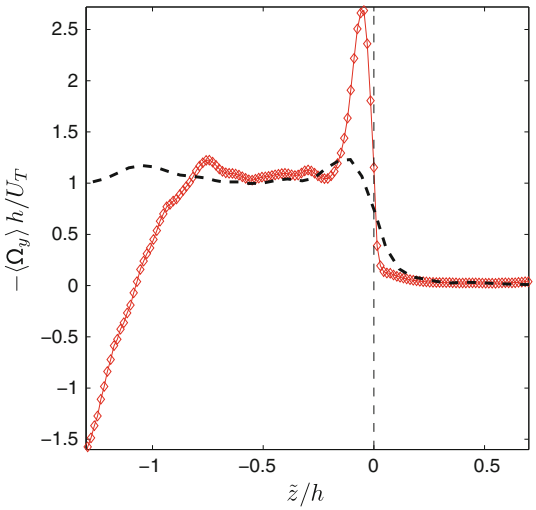

Fig. 15 Mean vorticity conditioned on the interface position (*red diamonds*) compared to data obtained in a unstratified jet flow by Westerweel et al. (2009) (*dashed black line*)

the vorticity spike. From the inset, the magnitude of the jump can be determined to be $\Delta U \approx 0.28 U_T$ which is consistent with the peak in $\langle\Omega_y\rangle$ and approximately twice as strong as the velocity jump observed in the jet ($\Delta U^{\text{jet}} \approx 0.18 U_T$). Interestingly, the slope of $\langle U\rangle$ within the turbulent region does not differ between the two flow types even though a considerable density gradient exists in this region at least in measurements evaluated in the laboratory frame (Odier et al. 2009). The conditional mean wall-normal velocity component is compared to the radial one of the jet in Fig. 16b, and both quantities are plotted such that positive values in the non-turbulent region imply a movement toward the interface. In both cases, the net flux outside the interface is toward the turbulent region. $\langle W\rangle$ remains positive throughout in the gravity current which is consistent with the speeding up of the flow closer to the wall observed in Fig. 10, whereas the streamwise decrease in centerline velocity in a jet leads to an outward flow in the center region. Given the relatively small tilt angle $\alpha = 10^{\circ}$, buoyancy forces predominantly affect vertical motions. This manifests itself in the fact that the wall-normal conditional velocity fluctuations (stars in Fig. 16c) reach much lower levels within the turbulent region than the streamwise ones (diamonds in Fig. 16c). From the inset in the figure, it can be seen that the ratios of the two components for the different flow types only diverge for $\tilde{z}/h < 0$, that is, inside the turbulent region. This also indicates that the stratification is limited to the turbulent zone while in the irrotational region the density is homogenous. The damped vertical fluctuations are also reflected in much lower values of the Reynolds stress component in comparison with the jet data (see Fig. 16d). In Fig. 16c, the wall-normal component on the turbulent side reaches a plateau around $\tilde{z}/h = -0.15$ but a possible 'jump' in the streamwise component at the same $\tilde{z}$-position is at best hinted at by a slight change of gradient. Even though non-zero fluctuations do exist outside the turbulent region, $\langle\tilde{u}\tilde{w}\rangle$ is very close to zero there as it should be for irrotational flow (Corrsin and Kistler 1954). The $\langle\tilde{u}\tilde{w}\rangle$-profile features a distinct jump at the interface with a magnitude of $\Delta\tau \approx 0.0076 U_T^2$ and again a width of 0.15 h. Peaks of the same extent in z-direction can also be found in the plot of the vorticity fluctuations (Fig. 16e) and the enstrophy transport, $\langle\tilde{\omega}_y^2 w\rangle$. The constant level of $\langle\tilde{\omega}_y^2\rangle^{1/2} \approx 0.5 h/U_T$ in the non-turbulent region suggests a noise level of about the same intensity. This puts the threshold value chosen in Sect. 2.3 into context, being about four times higher than this noise level. Apart from a sharper increase at the interface and a pronounced peak occurring just inside of it, the conditioned vorticity fluctuations of jet and gravity current are by and large comparable in the turbulent region. However, the situation is different for the enstrophy transport. First, the value of $\langle\tilde{\omega}_y^2 w\rangle$ outside the interface is reliably zero. This is remarkable in view of the fact that both $\langle\tilde{\omega}_y^2\rangle^{1/2}$ and $\langle\tilde{w}^2\rangle^{1/2}$ attain non-zero values in the non-turbulent region and underlines that vorticity fluctuations at $\tilde{z}/h > 0$ are truly due to measurement noise. The enstrophy transport is zero at $\tilde{z} = 0$ and therefore does not contribute to the advancement of the turbulent/non-turbulent interface. The same behavior was observed by Westerweel et al. (2009) and is explained by the fact that $\langle\omega_y^2 w\rangle$ implies purely convective transport of enstrophy, whereas it is known that the relative advancement of vorticity into irrotational fluid is governed by viscous quantities (Corrsin and Kistler 1954; Holzner and Lüthi 2011). Just inside the turbulent region, the transport of enstrophy in the gravity current is directed toward the non-turbulent region but falls behind the values reached in the jet passing the peak around $\tilde{z} = 0.1h$ presumably due to the lower vertical fluctuations or ultimately due to the effect of stratification.

With the exception of $\langle W\rangle$, all quantities were seen to undergo significant changes or 'jumps' within $-0.15h < \tilde{z} < 0$ such that, should an interface thickness be determined from this dataset, this seems to be the most natural choice. With even more confidence, it can be stated in light of Figs. 15 and 16a that 0.15 h is the thickness of a quite strong interfacial shear layer. This layer is covered by about 12 PIV data points and therefore fairly well resolved. To relate the thickness to other flow scales, the Taylor microscale $\lambda \approx u'\sqrt{15\nu/\epsilon}$ and the Kolmogorov scale $\eta \approx (\nu^3/\epsilon)^{1/4}$ are estimated using $\epsilon = u'^3/L$ and a measured integral scale of $L = 2.4$ cm. This results in $\lambda \approx 0.51$ cm and $\eta \approx 0.03$ cm such that the shear layer thickness of 0.15 h corresponds to about 2λ or 30η.

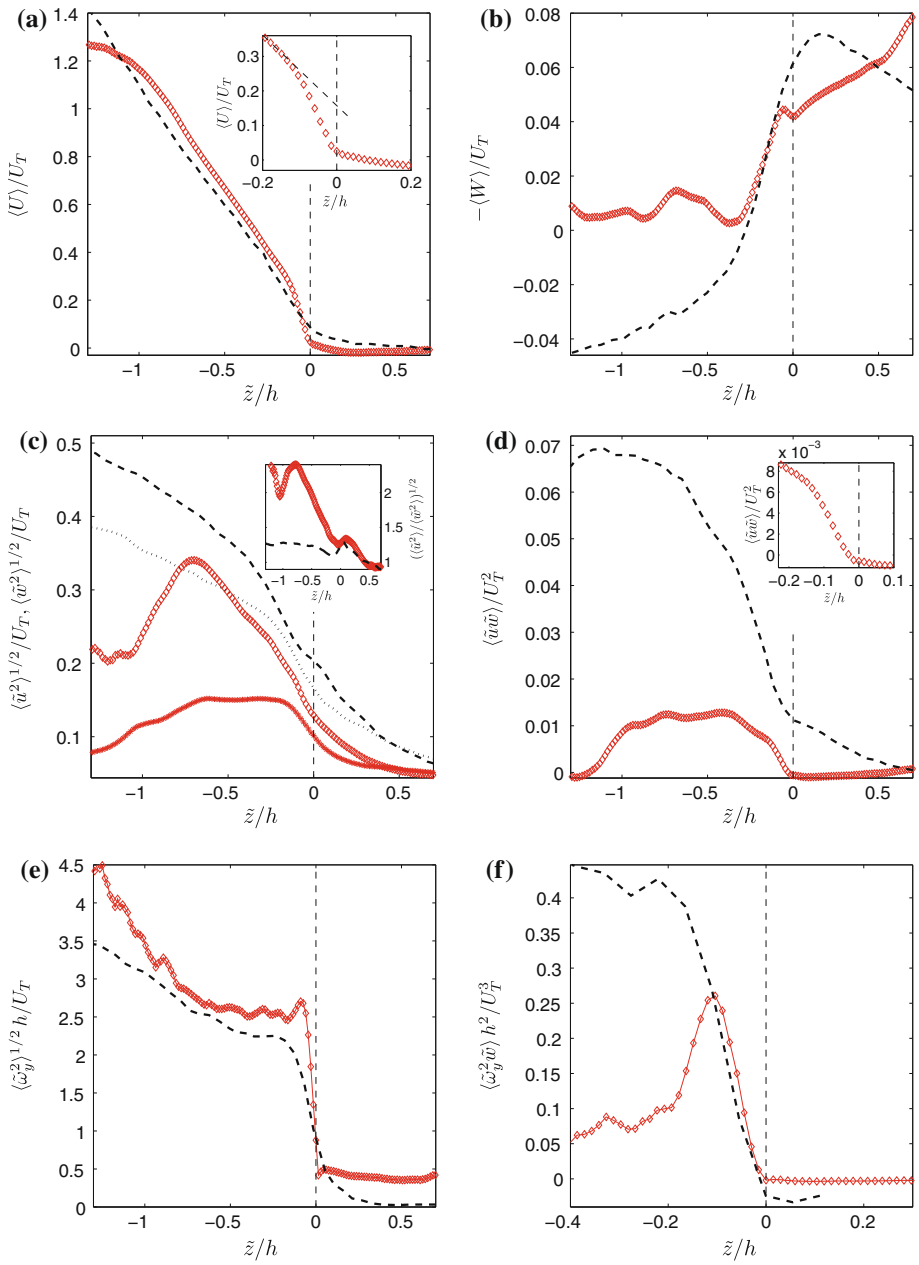

Fig. 16 **a–f** Collection of conditional profiles of various flow quantities obtained for the gravity current (*red symbols*) compared to those from a jet flow (*thick black lines*, taken from Westerweel et al. (2009)). Insets in **a** and **d** show magnifications of the region around the interface; the one in **c** displays the ratio of the two components presented in the main figure (*u*-component: *diamonds*, *dashed line*; *w*-component: *stars*, *dotted line*). Note the slightly changed limits of the *x*-axis in **f** focusing on the region around the interface

Since U_T is found to be independent of x, there is no contribution to the mean outward motion of the interface due to a slowing down of the mean flow as it can be observed in a jet flow. Assuming the mean interface to be approximately aligned with the x-axis, it follows that the mean vertical velocity at the interface is equal to the mean entrainment velocity and opposite and equal to the mean outward velocity of the interface E_b:

$$u_e = \langle W\rangle|_{\tilde{z}=0} = -E_b. \tag{10}$$

From Fig. 16b, it follows that $E_b = -u_e = 0.042U_T$ which is in excellent agreement with $u_e = -0.04U_T$ as determined from Eq. 4 previously and should be a fairly robust estimate of the entrainment velocity. From a control volume analysis, Westerweel et al. (2009) derive another expression to approximate E_b:

$$E_b \approx \frac{\Delta\tau}{\Delta U}. \tag{11}$$

With $\Delta\tau = 0.0076U_T^2$ and $\Delta U = 0.28U_T$, as determined above, this yields $E_b \approx 0.027U_T$ which is slightly off from the other two estimates for the same quantity. This is not surprising, because in a gravity current also buoyancy forces contribute to the momentum balance, on which Eq. 11 is based, and should be included. If we assume a density jump of thickness 0.15 h at the interface, which is

strongly suggested by the data in Fig. 16, an additional buoyancy term appears in the momentum balance such that Eq. 11 then reads

$$E_b \approx \frac{\Delta\tau + \sin\beta B}{\Delta U}. \quad (12)$$

The angle β between the mean interface and the horizontal can be estimated from $\beta \approx \alpha - \arctan E$ using $E = 0.04$. The buoyancy force integrated over the interface thickness is then $B = 0.15$ h g' if the density jump is assumed to be a step function or half that value for a linear gradient. The density jump necessary to yield $E_b = 0.04U_T$ from Eq. 12 would be approximately $0.5\Delta\rho_0$ or $\Delta\rho_0$ for the respective assumptions of the density profile. The latter value seems a bit high, but it should be safe to state that the data are consistent with the existence of a fairly strong density jump located at the TNTI. The situation is similar to the jumps of passive scalars observed by Bisset et al. (2002) and Westerweel et al. (2009), who also pointed out that, since usually the eddy diffusivity is much larger than the eddy viscosity, the scalar jump is generally more pronounced than the velocity jump. The fundamental difference, of course, to the present case is that the scalar here (the density) is an active one.

Following the analysis by Westerweel et al. (2009) further, a turbulent viscosity in the conditioned coordinate frame, $\tilde{\nu}_t$, can be defined by

$$\langle\tilde{u}\tilde{w}\rangle = -\tilde{\nu}_t \frac{\partial\langle U\rangle}{\partial\tilde{z}}, \quad (13)$$

again assuming the interface to be aligned with the x-axis in the mean and taking the value of $\frac{\partial\langle U\rangle}{\partial\tilde{z}} \approx 0.5U_T/h$ from the turbulent region in Fig. 16a. Convolution of $\tilde{\nu}_t(\tilde{z})$ with the histogram of the interface position allows to reconstruct the value of the turbulent viscosity in the laboratory frame at the mean interface position, $\nu_t(\overline{z^i})$ (e.g., Bisset et al 2002). This value is compared to $\nu_t(z) = l_m\left|\frac{\partial U}{\partial z}\right|$ resulting from the mixing length model in Fig. 17. As the figure shows, the values at the mean interface positions match fairly well consolidating the analysis in the laboratory frame with the one conditioned on the instantaneous interface position.

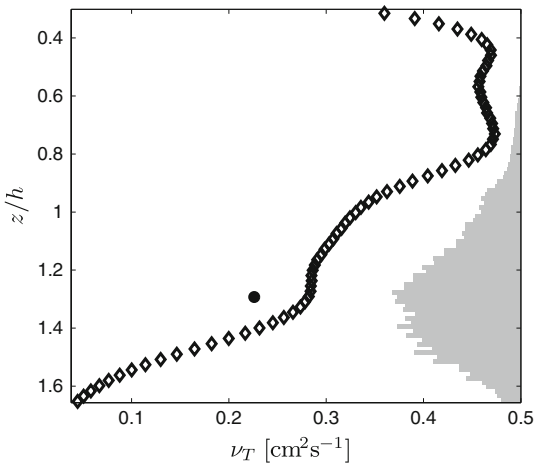

Fig. 17 Turbulent eddy viscosity obtained from the mixing length model (*open diamonds*) and according to Eq. 13 (*filled dot*). The bar plot on the *right-hand side* represents the histogram of the interface position

5 Conclusions

The paper describes a newly implemented gravity current setup operating at inflow Reynolds numbers of $Re_0 \approx 4{,}000$. Fluids of different densities were index matched to a degree that allowed PIV measurements without noticeable limitations at $\Delta\rho_0 = 2.5\,\mathrm{g\,l^{-1}}$. The treatment of the inflow is described in detail and measurements ensure its effectiveness in providing a turbulent uniformly distributed initial current at a steady flow rate up to $R_\lambda \approx 120$. Providing fluid along the bottom of the tank to compensate for the entrainment rate is seen to reduce backflow to a minimum without disturbing the irrotational flow outside the gravity current. Comparison of several quantities describing the flow field to a recent study by Odier et al. (2009) showed reasonable agreement and the effectiveness of the presented design in suppressing secondary flow. Further, dynamics at the turbulent/non-turbulent interface were studied in detail. Interfacial jumps were found to be generally more pronounced than in data of a jet flow reported by Westerweel et al. (2009) and occurred within 0.15 h of the interface. Most prominently, a very strong shear layer was seen to exist just inside the interface on the turbulent side exceeding the one found in jet flows in magnitude. Its width is about 2λ. Moreover, the wall-normal component of the turbulent velocity fluctuations was found to be damped by the effect of buoyancy within the turbulent region resulting in lower values of $\langle\tilde{u}\tilde{w}\rangle$ and of the vertical enstrophy transport by velocity fluctuations. In the non-turbulent region, the ratio of the two conditioned components of fluctuating velocity equals that of the jet suggesting that the density effects do not play any role outside of the turbulent region and that there exists a density jump across the shear layer. Weak but clearly non-zero velocity fluctuations were encountered outside the turbulent domain. In good agreement with a model put in place by Phillips (1955), they were observed to be irrotational apart from the measurement noise, and their cross-correlation $\langle\tilde{u}\tilde{w}\rangle$ was found to be zero. This can be interpreted as a validation for the interface detection scheme based on a threshold on enstrophy which seems superior to using a passive scalar such as dye. The mean entrainment velocity

was obtained in good agreement from Eqs. 4 and 10 yielding $u_e \approx -0.04U_T$, whereas the approximation by Eq. 11 and the fit by Turner (1986) (Eq. 5) resulted in lower magnitudes of $u_e = -0.027U_T$ and $u_e = -0.024U_T$. It could be shown that the consideration of buoyancy effects leads to an additional term in the control volume analysis on which Eq. 11 is based, and the assumed existence of a strong density jump at the TNTI yields better estimates of u_e. Lastly, results for the turbulent viscosity at the mean interface position stemming from the two strings of analysis followed in the paper—in laboratory frame and conditioned on the interface position—were seen to agree well.

Acknowledgments This work is sponsored by the Swiss National Science Foundation (SNF) under project number 200021/132567.

References

Anand R, Boersma B, Agrawal A (2009) Detection of turbulent/non-turbulent interface for an axisymmetric turbulent jet: evaluation of known criteria and proposal of a new criterion. Exp Fluids 47:995–1007. doi:10.1007/s00348-009-0695-5

Arneborg L, Fiekas V, Umlauf L, Burchard H (2007) Gravity current dynamics and entrainment - a process study based on observations in the Arkona basin. J Phys Oceanogr 37:2094–2113. doi:10.1175/JPO3110.1

Bisset DK, Hunt JCR, Rogers MM (2002) The turbulent/non-turbulent interface bounding a far wake. J Fluid Mech 451:383–410. doi:10.1017/10.1017/S0022112001006759

Chen J, Odier P, Rivera M, Ecke R (2007) Laboratory measurement of entrainment and mixing in oceanic overflows. ASME Conf Proc 2007(42894):1283–1292. doi:10.1115/FEDSM2007-37673

Corrsin S, Kistler A (1954) The free-stream boundaries of turbulent flows. NACA TN-3133, TR-1244:1033–1064

Daviero GJ, Roberts PJW, Maile K (2001) Refractive index matching in large-scale stratified experiments. Exp Fluids 31:119–126. doi:10.1007/s003480000260

Ellison TH, Turner JS (1959) Turbulent entrainment in stratified flows. J Fluid Mech 6(03):423–448. doi:10.1017/S0022112059000738

Holzner M, Lüthi B (2011) Laminar Superlayer at the Turbulence Boundary. Phys Rev Lett 106(13):134503. doi:10.1103/PhysRevLett.106.134503

Holzner M, Liberzon A, Guala M, Tsinober A, Kinzelbach W (2006) Generalized detection of a turbulent front generated by an oscillating grid. Exp Fluids 41:711–719. doi:10.1007/s00348-006-0193-y

Legg S, Briegleb B, Chang Y, Chassignet EP, Danabasoglu G, Ezer T, Gordon AL, Griffies S, Hallberg R, Jackson L, Large W, Özgökmen TM, Peters H, Price J, Riemenschneider U, Wu W, Xu X, Yang J (2009) Improving oceanic overflow representation in climate models: the gravity current entrainment climate process team. B Am Meteorol Soc 90:657–670. doi:10.1175/2008BAMS2667.1

Mathew J, Basu AJ (2002) Some characteristics of entrainment at a cylindrical turbulence boundary. Phys Fluids 14(7):2065–2072. doi:10.1063/1.1480831

McDougall TJ (1979) On the elimination of refractive-index variations in turbulent density-stratified liquid flows. J Fluid Mech 93(1):83–96. doi:10.1017/S0022112079001798

Odier P, Chen J, Rivera MK, Ecke RE (2009) Fluid mixing in stratified gravity currents: The Prandtl mixing length. Phys Rev Lett 102:134504. doi:10.1103/PhysRevLett.102.134504

Odier P, Chen J, Ecke R (2012) Understanding and modeling turbulent fluxes and entrainment in a gravity current. Phys D 241(3):260–268. doi:10.1016/j.physd.2011.07.010

Philip J, Marusic I (2012) Large-scale eddies and their role in entrainment in turbulent jets and wakes. Phys Fluids 24(5):055108. doi:10.1063/1.4719156

Phillips OM (1955) The irrotational motion outside a free turbulent boundary. Math Proc Cambridge 51:220–229. doi:10.1017/S0305004100030073

Rahmstorf S (2002) Ocean circulation and climate during the past 120,000 years. Nature 419(6903):207–214

da Silva CB, Taveira RR (2010) The thickness of the turbulent/nonturbulent interface is equal to the radius of the large vorticity structures near the edge of the shear layer. Phys Fluids 22(12):121702. doi:10.1063/1.3527548

Simpson JE (1999) Gravity currents. Cambridge University Press, Cambridge

Smyth WD, Moum JN (2000) Length scales of turbulence in stably stratified mixing layers. Phys Fluids 12(6):1327–1342. doi:10.1063/1.870385

Turner JS (1986) Turbulent entrainment—the development of the entrainment assumption, and its application to geophysical flows. J Fluid Mech 173:431–471. doi:10.1017/S0022112086001222

Westerweel J, Hofmann T, Fukushima C, Hunt JCR (2002) The turbulent/non-turbulent interface at the outer boundary of a self-similar turbulent jet. Exp Fluids 33:873–878. doi:10.1007/s00348-002-0489-5

Westerweel J, Fukushima C, Pedersen JM, Hunt JCR (2009) Momentum and scalar transport at the turbulent/non-turbulent interface of a jet. J Fluid Mech 631:199–230. doi:10.1017/S0022112009006600

Wolf M, Lüthi B, Holzner M, Krug D, Kinzelbach W, Tsinober A (2012) Investigations on the local entrainment velocity in a turbulent jet. Phys Fluids 24(10):105110. doi:10.1063/1.4761837